Available online at www.sciencedirect.com

ScienceDirect

Geochimica et Cosmochimica Acta 328 (2022) 120–129

Geochimica et Cosmochimica Acta

www.elsevier.com/locate/gca

Clumped isotope signatures of nitrous oxide formed by bacterial denitrification

Kristýna Kantnerová [a,b,*,1], Shohei Hattori [c,d], Sakae Toyoda [d], Naohiro Yoshida [d,e,f], Lukas Emmenegger [a], Stefano M. Bernasconi [b], Joachim Mohn [a]

[a] *Empa, Laboratory for Air Pollution/Environmental Technology, 8600 Dübendorf, Switzerland*
[b] *ETH Zurich, Department of Earth Sciences, 8092 Zurich, Switzerland*
[c] *Nanjing University, International Center for Isotope Effects Research, School of Earth Sciences and Engineering, 210023 Nanjing, China*
[d] *Tokyo Institute of Technology, Department of Chemical Science and Engineering, Yokohama 226-8503, Japan*
[e] *Tokyo Institute of Technology, Earth-Life Science Institute (ELSI), Tokyo 152-8550, Japan*
[f] *National Institute of Information and Communications Technology (NICT), Tokyo 184-8795, Japan*

Received 28 May 2021; accepted in revised form 4 May 2022; Available online 13 May 2022

Abstract

Multiply substituted isotopic species of nitrous oxide (N_2O), referred to as clumped isotopes, represent a promising new tool for distinguishing production pathways of this potent greenhouse gas. This work presents the first determination of enrichment factors of N_2O clumped isotopes during bacterial denitrification. Samples of N_2O obtained after 1-, 3-, and 7-day incubations of a pure culture of the denitrifier *Pseudomonas aureofaciens* at 20 °C and 30 °C were analysed by the recently developed quantum cascade laser absorption spectroscopy (QCLAS) method. Enrichment factors $\varepsilon_{p/s}$ of the cumulative product (p) relative to the substrate (s) were determined using a Rayleigh model for the seven most abundant isotopically substituted molecules (isotopocules) of N_2O. Values of the enrichment factors $\varepsilon_{p/s}$ (with uncertainty expressed as expanded standard uncertainty at the 95% confidence interval) at the two incubation temperatures (20 °C/30 °C) are:

$^{14}N^{15}N^{16}O$ (456): $\varepsilon_{456} = (-40.3 \pm 2.6)‰/(-35.1 \pm 0.7)‰$
$^{15}N^{14}N^{16}O$ (546): $\varepsilon_{546} = (-38.1 \pm 3.4)‰/(-31.2 \pm 0.6)‰$
$^{14}N^{14}N^{17}O$ (447): $\varepsilon_{447} = (21.3 \pm 1.2)‰/(24.5 \pm 0.5)‰$
$^{14}N^{14}N^{18}O$ (448): $\varepsilon_{448} = (38.8 \pm 1.5)‰/(46.4 \pm 1.2)‰$
$^{14}N^{15}N^{18}O$ (458): $\varepsilon_{458} = (-8.9 \pm 2.0)‰/(-11.7 \pm 0.6)‰$
$^{15}N^{14}N^{18}O$ (548): $\varepsilon_{548} = (-3.4 \pm 1.1)‰/(-1.8 \pm 0.5)‰$
$^{15}N^{15}N^{16}O$ (556): $\varepsilon_{556} = (-85.9 \pm 1.5)‰/(-63.9 \pm 1.4)‰$

Temporal evolutions of the abundances of singly substituted N_2O isotopocules during nitrate reduction agree with previously published experiments: there is normal isotope effect associated with the production of $^{14}N^{15}N^{16}O$ and $^{15}N^{14}N^{16}O$; i.e., intermediates leading to $^{14}N^{14}N^{16}O$ react faster than intermediates leading to $^{14}N^{15}N^{16}O$ and $^{15}N^{14}N^{16}O$. However, the production of $^{14}N^{14}N^{17}O$ and $^{14}N^{14}N^{18}O$ is associated with inverse isotope effect; i.e., intermediates leading to $^{14}N^{14}N^{16}O$ react slower than intermediates leading to $^{14}N^{14}N^{17}O$ and $^{14}N^{14}N^{18}O$ due to preferential cleavage of ^{16}O during nitrate reduction

* Corresponding author at: Empa, Laboratory for Air Pollution/Environmental Technology, 8600 Dübendorf, Switzerland.
E-mail addresses: kristyna.kantnerova@alumni.ethz.ch (K. Kantnerová), hattori@nju.edu.cn (S. Hattori), toyoda.s.aa@m.titech.ac.jp (S. Toyoda), yoshida.n.aa@m.titech.ac.jp (N. Yoshida), lukas.emmenegger@empa.ch (L. Emmenegger), stefano.bernasconi@erdw.ethz.ch (S.M. Bernasconi), joachim.mohn@empa.ch (J. Mohn).
[1] Present address: Department of Geological Sciences, University of Colorado Boulder, 80301 Boulder, CO, USA.

https://doi.org/10.1016/j.gca.2022.05.006
0016-7037/

to N_2O. Isotopic fractionation at the incubation temperature of 30 °C was significantly lower compared to 20 °C. We observed a large kinetic isotope effect of the ^{15}N site preference (SP) and the $^{15}N—^{18}O$ site preference (SP^{18}) at the onset of the reaction. SP^{18} was found to be closer to 0‰ than SP, which is thought to arise from similar rates of breakage of the $^{15}N—O$ and $^{14}N—O$ bonds in the reaction intermediates. The $^{15}N—^{18}O$ clumped isotope anomalies in two isotopic isomers (isotopomers) $^{14}N^{15}N^{18}O$ and $^{15}N^{14}N^{18}O$ ($\Delta_{avg}^{458+548}$) follow a temporal trend similar to those of SP and SP^{18}. The $^{15}N—^{15}N$ clumped isotope anomalies in $^{15}N^{15}N^{16}O$ are greater than 0‰ and show no clear temporal trend or influence of incubation temperature, suggesting no strong combinatorial effects involved during the N—N bond formation. Overall, our data illustrate that clumped N_2O isotopes may be used as independent tracers for reaction mechanisms of N_2O conversion and may establish themselves as a worthwhile tool to study the biogeochemical cycle of N_2O.

Keywords: Clumped isotopes; Nitrous oxide; Denitrification; *Pseudomonas aureofaciens*; QCLAS; Isotopic analysis; Isotopic fractionation; Fractionation constants; Reaction mechanism; NO reduction; cNOR

1. INTRODUCTION

In natural ecosystems, the ozone-depleting greenhouse gas nitrous oxide (N_2O) is formed by multiple microbial and abiotic pathways, but the majority of N_2O emissions is generally attributed to two microbial processes: denitrification and nitrification (Butterbach-Bahl et al., 2013). Distinct pathways yield a particular isotopic composition of the formed N_2O due to different associated kinetic isotopic fractionations (Toyoda et al., 2017); thus, high-precision measurements of isotope ratios can discriminate between processes. To determine the source of N_2O, the measurement of the isotope ratio of singly isotopically substituted molecules (isotopocules) expressed in δ values (in ‰) is usually employed:

$$\delta = \frac{R_{sample}}{R_{reference}} - 1, \quad (1)$$

where R is the isotope abundance ratio ($^{15}N/^{14}N$, $^{17}O/^{16}O$, or $^{18}O/^{16}O$) in a sample or an international isotopic reference material (Air-N_2 for N, VSMOW for O). In addition to variations in bulk isotope composition, there is a tendency for the heavier ^{15}N isotope to be enriched at the central (α) N position in the asymmetric N_2O molecule, $^{\beta}N–^{\alpha}N–O$, under equilibrium conditions (Wang et al., 2004). This tendency is defined as the ^{15}N site preference (SP): $SP = \delta^{456} - \delta^{546}$. The labels 456 and 546 denote shorthand notations for isotopic isomers (isotopomers) $^{14}N^{15}N^{16}O$ and $^{15}N^{14}N^{16}O$, respectively. For natural N_2O sources, values of SP differ due to varying isotopic fractionation at active centres of enzymes that are involved in N_2O formation and have shown potential for identifying specific formation mechanisms (Toyoda et al., 2017).

N_2O production by denitrifying microorganisms, e.g. archaea, fungi, and bacteria, involves stepwise enzymatic reduction of soil nitrate (NO_3^-) or nitrite (NO_2^-) through nitric oxide (NO) to N_2O (Zumft, 1997). The crucial steps with respect to N_2O formation and its isotopic composition are the N–N bond formation between two NO molecules and the subsequent cleavage of one O atom, catalysed by the NO reductase (NOR). To the best of our knowledge, the reaction mechanisms of the NO reduction step in denitrification remain inconclusive. Three mechanisms have been proposed for the bacterial NO reduction by the cNOR enzyme (Watmough et al., 2009; Hino et al., 2010). The *trans* mechanism, which is typically favoured in the literature, describes parallel binding of two NO molecules to the heme b_3-Fe and non-heme Fe_B and the subsequent formation of the N–N bond with *trans* symmetry of the reaction intermediate with respect to the N–N bond (Fig. 1 left). In the other two proposed reaction mechanisms, the NO molecules are bound in series: 1) either solely to non-heme Fe_B, which is known as the *cis* Fe_B mechanism (Fig. 1 middle) and supported by UV/Vis, EPR, and Mössbauer spectroscopy (Timóteo et al., 2011); or 2) solely to heme b_3-Fe, known as the *cis* heme b_3 mechanism (Fig. 1 right) and implicated by density functional theory (DFT) calculations (Blomberg et al., 2006; Blomberg, 2017). In both mechanisms, a *cis* isomeric structure of the reaction intermediate is predicted, with respect to the N–N bond. The final reaction step in denitrification is N_2O reduction to dinitrogen (N_2), which occurs only if the N_2O reductase (N_2OR) is expressed in the respective microbial strain.

The bulk $^{15}N/^{14}N$ ratio of N_2O reflects that of the N substrate (Sigman et al., 2001), while the $^{18}O/^{16}O$ signature is more complex. It can be affected by O-exchange or equilibration between reaction intermediates and water (H_2O), as well as isotope effects related to the fate of the oxygen isotopes at a branching point of the reaction. In the reaction chain, oxygen atoms can be either transferred to the subsequent nitrogen species or be lost as H_2O, an effect called the "branching isotope effect" (Casciotti et al., 2007). The site-specific isotopic composition of the produced N_2O is expected to vary based on the reaction mechanism of the NO reduction step (Fehling, 2012). For the *trans* mechanism, binding of the two NO molecules to the Fe and Fe_B is equivalent, and therefore the isotopomers 456–546 and 458–548 ($^{14}N^{15}N^{18}O$–$^{15}N^{14}N^{18}O$) are expected to be formed with a similar probability, making SP and SP^{18} close to 0‰. In the absence of N_2O reduction, N_2O originating from bacterial denitrification has been observed to display SP values around 0‰ or slightly negative (Sutka et al., 2006). Negative SP values can be caused by a slight preference for ^{15}N to bind to the Fe atom that binds the N atom that becomes the future terminal N in the formed N_2O. Another explanation for negative SP is isotopic fractionation during breaking of the O–N bond in the symmetric O–NNO species (He et al., 2020) that is small and

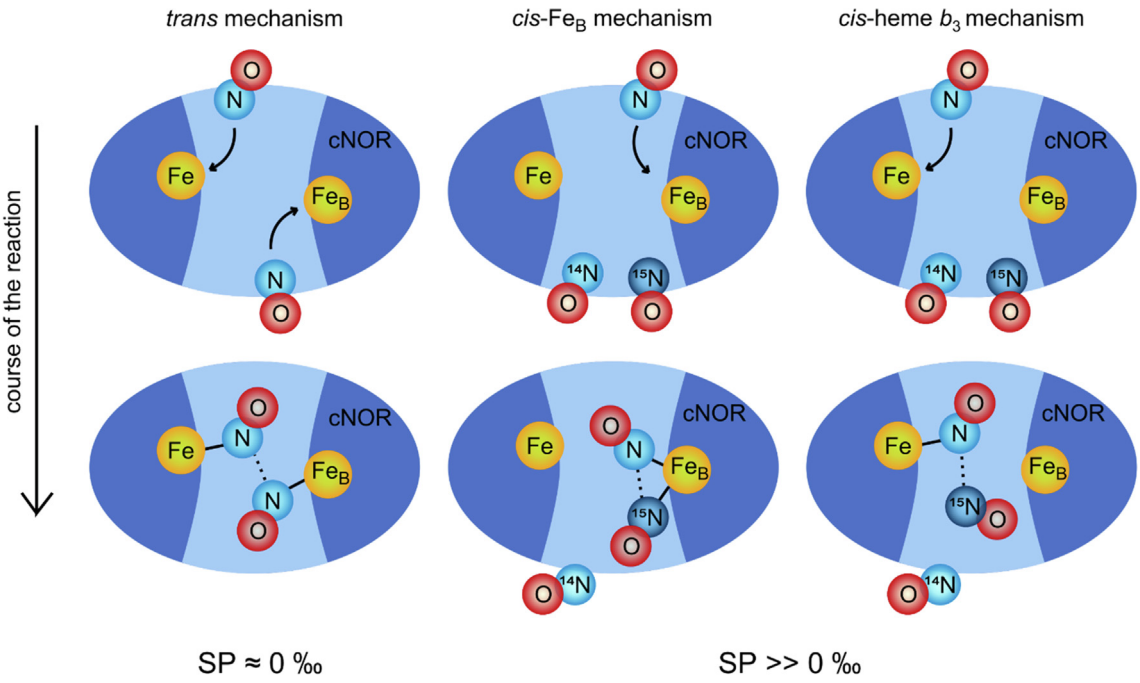

Fig. 1. An illustration of suggested mechanisms for ON–NO coupling by the cNOR enzyme (based on information in Watmough et al. (2009)) and expected SP values. The *cis* mechanisms also depict a preference for ^{15}NO as the second NO molecule in the N–N bond formation.

inverse (^{16}O–^{15}N slightly more probable to be broken than ^{16}O–^{14}N), resulting in slightly higher production of 546 than 456 (SP < 0‰). In the *cis* mechanism, the binding of the second NO molecule to the first one is expected to be affected by a positive ^{15}N fractionation effect and to result in highly positive SP values. This is sometimes compared to the mechanism of N_2O produced by fungal denitrification with SP around 37‰, with the P450nor enzyme having one Fe in the centre (Sutka et al., 2008). In spite of a relatively good understanding of these isotope effects, the use of bulk and site-specific isotope ratios in singly substituted isotopocules to distinguish N_2O formed in denitrification from other N_2O sources is limited, because different processes lead to similar isotopic signatures; e.g. fungal denitrification and hydroxylamine oxidation (Toyoda et al., 2017), or bacterial denitrification and nitrifier-denitrification (Sutka et al., 2003; Frame and Casciotti, 2010).

"Clumped isotope geochemistry" – the study of variation in abundance of the very rare molecules containing more than one of the rare isotopes of one or more elements – is a promising new tool that is expected to facilitate N_2O source attribution by offering new isotopic dimensions (e.g. Eiler, 2013). Under equilibrium conditions, the bonding of two heavier isotopes in a molecule (denoted as clumping) is thermodynamically favoured, and thus their chemical bond is more stable (Wang et al., 2004). Also, the extent of clumping tends to increase with decreasing temperature. Therefore, for samples that are formed under equilibrium, the clumped isotope content can be used as a proxy for their formation temperature (Eiler, 2007). This has been applied for example in carbonate palaeothermometry to access new information about Earth's past climates (e.g. van Dijk et al. 2020), or in studies of low-temperature biogenic and high-temperature thermogenic sources of methane (e.g. Stolper et al., 2015; Wang et al., 2015). Likewise, the abundance of $^{18}O_2$ in polar firn and ice was introduced as a proxy for past levels of ozone (O_3) in the troposphere, as O_3 photochemistry equilibrates the isotopic distribution in O_2 (Yeung et al., 2019b).

Besides equilibration temperature, clumped isotope signatures were found to record a variety of other parameters related to the generation and history of a compound. Under the non-equilibrium conditions of biologically mediated chemical reactions, isotopic distribution in molecules is mostly governed by kinetic isotope fractionation. In this case, clumped isotopes can offer insight into reaction mechanisms, reaction reversibility and/or substrate identity (e.g. Wang et al., 2015). For example, biological formation of O_2 is a non-equilibrium process, as O_2 produced by photosynthesis has lower abundances of the clumped isotopocules $^{18}O_2$ and $^{17}O^{18}O$ than those calculated for equilibrium conditions (Yeung et al., 2015). This effect, rooted in the statistics of pairing atoms and referred to as a combinatorial effect, occurs when two halves of an atom pair are assembled with different isotopic preferences or drawn from different reservoirs (Yeung, 2016). The abundance of $^{15}N_2$ isotopocules, accompanied by modelling, has been applied to constrain and quantify biological production of N_2 in situ in natural soils (Yeung et al., 2019a), to study nitrogen chemistry at planetary scale (Yeung et al., 2017), or to constrain sources of nitrogen in the Earth's mantle (Labidi et al., 2020).

While there is a growing body of literature on the factors controlling the abundance of the clumped isotope species of CO_2, CH_4, N_2 and O_2, N_2O remains an understudied gas. Theoretical studies show that, as with the singly substituted

isotopomers 456–546, 458 is favoured over 548 under equilibrium conditions at any temperature (and $^{14}N^{15}N^{17}O$ over $^{15}N^{14}N^{17}O$) (Wang et al., 2004; Cao and Liu, 2012). The ^{15}N affinity for the central N position results in a complex relationship between equilibrium clumped isotope signatures and temperature, yielding large signals; e.g. 46‰ enrichment of 458 over 548 at 300 K (Wang et al., 2004). In parallel to the established SP, the clumped isotope signature SP^{18} is used to express this enrichment: $SP^{18} = \delta^{458} - \delta^{548}$. The equilibrium abundance of 556 ($^{15}N^{15}N^{16}O$) is governed by different temperature behaviours of the isotopomers 456 and 546, resulting in only a small enrichment at 300 K (Wang et al., 2004). The abundances of the clumped species 458, 548, and 556 in N_2O are expressed in Δ values; e.g., Δ^{458} represents the 458/446 ratio relative to the stochastic distribution of ^{14}N, ^{15}N, ^{16}O, ^{17}O, and ^{18}O within the N_2O pool. A detailed description of the Δ notation used here can be found in the Methods subsection.

In addition to equilibrium thermodynamics, Δ^{458}, Δ^{548} and Δ^{556} record information about the reaction mechanism, reversibility, transport processes, and mixing. First experimental data on the clumped isotope signatures of N_2O produced by microbial denitrification were published by Magyar et al. (2016). The authors obtained few data regarding the site preference of ^{15}N in relation to ^{18}O ($SP^{18} = -0.5 \pm 3.8$‰) or the average content of two clumped isotopomers 458 and 548 (0.39 ± 0.40‰). Furthermore, Δ^{556} was not quantified, probably due to mass interferences with $^{12}C^{18}O^{16}O$ during isotope-ratio mass spectrometry (IRMS) analysis. Generally, the Δ^{556} signature is a product of the difference in ^{15}N abundance between moieties involved in the N–N bond formation and related kinetic isotope effects (Yeung, 2016). Based on Yeung (2016), Δ^{556} values are predicted to be depleted up to 0.6‰ due to possible combinatorial effects during the N–N coupling. Regarding clumped N_2O isotopes in denitrification, it has been hypothesised that: 1) similar to SP, SP^{18} reflects the characteristic signature for the transition state during the N–N bond formation and the N–O bond cleavage (distinguishing between the *cis* or *trans* structure of intermediates); 2) Δ^{458} and Δ^{548} are characteristic signatures for the N substrate, its transformations and equilibration of denitrification intermediates with H_2O (Magyar et al., 2016); or 3) similar to SP^{18}, Δ^{556} captures information about kinetics, transition state, and combinatorics that are subject to the N–N bond formation (Yeung, 2016; Toyoda et al., 2017). A comprehensive understanding of clumped isotope signatures from kinetically governed reactions is currently missing due to the complex relationship of effects, the lack of theoretical models, and, most importantly, the very limited experimental data available (Kaiser et al., 2003; Magyar et al., 2016; Kantnerová et al., 2020b; Kantnerová et al., 2020a).

The aim of this study is to provide clumped isotope signatures Δ^{458}, Δ^{548}, and Δ^{556} of N_2O produced by the denitrifying bacteria *Pseudomonas aureofaciens*. This strain lacks the N_2OR enzyme and, therefore, quantitatively converts NO_3^- to N_2O without further reduction to N_2. We apply a laser spectroscopic technique with an independent calibration approach, which extends the current analytical toolbox over standard IRMS. Results are expected to allow for evaluation of the use of clumped N_2O isotopes as an independent tool for mechanistic studies on the N_2O cycle once more detailed models become available. The hypotheses presented here are based on currently available estimates of clumped isotope behaviour. In future, a more detailed model using high-level *ab initio* methods must be developed for clumped N_2O isotopes, as those methods provide better absolute accuracy (Raman et al., 2005) compared to, e.g., the quantum chemical approach using continuum models that was applied by Fehling (2012).

2. METHODS

2.1. Denitrifier incubation

The denitrifier *Pseudomonas aureofaciens* (ATCC 13985) was incubated at either 20 °C or 30 °C for 1, 3, or 7 days to convert the NO_3^- in the medium to N_2O, following the method described in Hattori et al. (2016). Tryptic soy broth (TSB, volume 1 L) was prepared in media bottles with 36 mmol KH_2PO_4, 10 mmol KNO_3, and 7.5 mmol NH_4Cl, and sealed with aluminium-capped butyl septa. The total volume of the liquid phase was 44 mL for the intermediate medium and 440 mL for the reaction medium. The medium bottles were autoclaved at 121 °C for 30 min (intermediate medium) or 50 min (reaction medium) and allowed to cool overnight in the autoclave. A strain of denitrifier *P. aureofaciens* was grown for 2 days in the intermediate medium. The bottles were placed in an incubator shaker (60 rpm) at 30 °C. The bottles with reaction medium were inoculated afterwards with 2 mL of the denitrifier solution from the intermediate medium. They were kept in the incubator shaker at either 20 °C or 30 °C to convert NO_3^- to N_2O. N_2O was collected after 1, 3, or 7 days to obtain the product at different stages of the reaction progress. Each experiment was duplicated under the specified reaction conditions.

2.2. Sampling of N_2O

N_2O produced during incubations was purged from the medium with high–purity helium (He, 99.9995%) at a flow rate of 100 mL/min for 44 min, which is equivalent to ten times the volume of the medium. The gas was purified using a pre-concentration line built in-house (Fig. A.1) by being passed through 300 mL of 1 M NaOH solution in a gas-washing bottle to remove CO_2, then a permeation dryer (MD-050-72S-2 Perma Pure, Dr. Marino Müller AG, Switzerland; with counter-flow of dry air at 500 mL/min) to dehumidify the gas, and an Ascarite (Sigma Aldrich, Switzerland) trap bracketed by magnesium perchlorate (Fisher Scientific AG, Switzerland) to remove residual CO_2 and H_2O. Sampled N_2O was frozen into a stainless-steel loop immersed in liquid N_2. The gas flow was monitored at the outlet of the line by a mass-flow meter (red-y compact, Vögtlin Instruments GmbH, Switzerland). After the sampling, He and other trace gases with low boiling points were removed by evacuation, before the collected N_2O was cryogenically transferred into a 50 mL

stainless-steel cylinder (ARBOR Fluidtec AG, Switzerland). Prior to the analysis, the samples were diluted with N_2 (99.9999%) to approx. 1.55% N_2O.

2.3. QCLAS analysis

The analytical setup consisted of a spectrometer using quantum cascade laser absorption spectroscopy (QCLAS) and an automated gas inlet system (both Aerodyne Research, Inc., USA). Calibration and sample gases were introduced separately through the inlet system (approx. 10 mL at standard temperature and pressure, i.e., approx. 6 μmol of N_2O in N_2 per analysis) into a pre-evacuated optical cell of the QCLAS instrument. The pressure in the optical cell was adjusted by filling an intermediate volume of 50 mL (±20 mL) with a calibration or sample gas to a pre-set pressure. The gas was then expanded into the pre-evacuated cell, which was then closed, and an absorption spectrum was measured. The leak rate of the optical cell was 40 Pa/h, which is negligible for the duration of the gas analysis (2.5 min). A measurement cycle (42 min) consisted of the analysis of the sample gas bracketed by analyses of three calibration gases (CG; a sequence of CG1-CG2-CG3-sample-CG1-CG2-CG3); this cycle was then repeated three times for every sample. Between the individual analyses, the optical cell and the inlet system were evacuated for 90 s, flushed with N_2 (99.9999%), and then evacuated for another 90 s. A more detailed description of the analytical technique can be found in Kantnerová et al. (2020a) and Kantnerová et al. (2020b).

2.4. Data analysis

The N_2O yield was determined gravimetrically after purification by comparing weights of empty 50 mL stainless-steel cylinders with weights of the same cylinders filled with the purified N_2O. The δ and Δ values for the sample gases were calculated using the mole-fraction calibration scheme described in Kantnerová et al. (2020b). The calibration gases span a concentration range of 1.50 – 1.85% N_2O in N_2. The gases share the same isotopic composition: $\delta^{456} = (-0.11 \pm 0.20)‰$, $\delta^{546} = (0.95 \pm 0.21)‰$, $\delta^{448} = (38.57 \pm 0.25)‰$, $\Delta^{458} = (-0.06 \pm 0.80)‰$, $\Delta^{548} = (0.49 \pm 0.46)‰$, $\Delta^{556} = (-0.88 \pm 1.76)‰$. The given uncertainties are expanded uncertainties at the 95% confidence interval. The δ values were determined against reference gases that are anchored to $^{15}N/^{14}N$ ratios of Air-N_2 and $^{18}O/^{16}O$ and $^{17}O/^{16}O$ ratios of VSMOW by Sakae Toyoda, Tokyo Institute of Technology (Toyoda et al., 1999). The Δ values are given relative to the calculated stochastic distribution and were standardised by heating the working standard in the presence of aluminium oxide at 100 °C and 200 °C (more details in Magyar et al. (2016) and Kantnerová et al. (2020b)). The mass-independent behaviour of O isotopes was evaluated by calculating $\Delta^{17}O$, where $\Delta^{17}O = \delta^{18}O - 0.516\,\delta^{17}O$ (Werner and Brand, 2001).

Enrichment factors $\varepsilon_{p/s}$ of the cumulative product (p) relative to the substrate (s) describe isotope fractionation effects during a reaction. The enrichment factors were calculated using the Rayleigh model following definitions for $\varepsilon_{p/s}$ in Mariotti et al. (1981) and Sutka et al. (2006). Changes in the isotopic composition during denitrification (the Rayleigh model) were described following Sutka et al. (2006) and fitted using $[x]$ vs. δ plots:

$$y = a + b[x] \tag{2}$$

where y is the δ value, a and b are coefficients estimated by fitting using the accumulated product model, and the variable $[x]$ represents the course of the reaction (1: reaction start, 0: reaction end) (Sutka et al., 2006):

$$[x] = -f\,\frac{\ln(f)}{1-f} \tag{3}$$

where f is the fraction of the remaining substrate:

$$f = 1 - \frac{2n_{N_2O}}{n_{NO_3^-,0}} \tag{4}$$

Here, n is the molar amount of accumulated product N_2O and initial substrate NO_3^-. The slope b in Eq. (2) corresponds to the enrichment factor $\varepsilon_{p/s}$ (Sutka et al., 2006). The fractionation factor α, which is defined as a ratio of the rate constants of the heavy (k_2) and the light (k_1) isotopocules (Haslun et al., 2018), can be calculated using Eq. (5):

$$\alpha = \varepsilon_{p/s} + 1 \tag{5}$$

An example of the Rayleigh fractionation plots for δ^{458} can be found in the Supplementary information (Fig. A.2). Fitting and calculation of confidence intervals was performed using York's method (York, 1969). The intercept (a) and slope (b), as well as 95% confidence intervals, were calculated by including the standard deviation on both $[x]$ (estimated from the gravimetric determination) and y data (obtained from the QCLAS analysis).

2.5. Notation for clumped N_2O isotopes

The abundance of the clumped isotopocules is usually referenced to the stochastic distribution of isotopes and given in Δ values. The definition of the Δ values derives from a set of isotope-exchange equilibrium reactions between all twelve N_2O isotopocules (Wang et al., 2004); e.g. for Δ^{556}:

$$^{14}N^{14}N^{16}O + {}^{15}N^{15}N^{16}O \leftrightarrow {}^{14}N^{15}N^{16}O + {}^{15}N^{14}N^{16}O \tag{6}$$

This isotope-exchange reaction can be described by the equilibrium constant K using concentration of the involved isotopocules (square brackets):

$$K = \frac{[456][546]}{[446][556]} \tag{7}$$

The value of K is temperature-dependent; in general, a temperature increase drives the isotopic equilibrium to the right, leading to a decrease of the abundance of the clumped species. The Δ variable is defined in accordance with e.g. Ono et al. (2014) and Prokhorov et al. (2019); the full, detailed derivation can be found in Kantnerová (2020):

$$\Delta^{556} \equiv -\ln\left(\frac{K}{K^*}\right) = \left(\frac{R^{556}}{R^{556*}} - 1\right) - \left(\frac{R^{456}}{R^{456*}} - 1\right) - \left(\frac{R^{546}}{R^{546*}} - 1\right) \quad (8)$$

R^{556} is the ratio of the abundance of the 556 species to that of the 446 species in a sample; R^{556*} is the ratio of the abundance in the same sample but with stochastic isotopic distribution (the reference point; similarly for 456 and 546). The Δ^{556} values were referenced against a working standard gas according to Eq. (11) in Kantnerová et al. (2020b), and in a similar manner for Δ^{458} and Δ^{548}.

3. RESULTS

After 1-, 3-, and 7-day incubations of *P. aureofaciens*, the N_2O yields were approx. 2%, 65%, and 90% at 20 °C and 5%, 90%, and 100% at 30 °C, respectively. Due to the limited amount of N_2O, the gas samples from the 1-day incubations conducted at 20 °C were not analysed. The gas samples from duplicated 1-day incubations conducted at 30 °C were combined and the QCLAS analysis was run twice (two triplicate analyses), but on one combined sample only. Other sample gases were analysed in the standard way, i.e., one triplicate analysis per each duplicated sample.

The enrichment factors $\varepsilon_{p/s}$ derived from the Rayleigh model using Eq. (2)–(4) are summarised in Table 1. The isotopocules 456, 546, 458, and 556 have negative $\varepsilon_{p/s}$ values, indicating normal isotopic fractionation. The isotope effect for 556, ε_{556}, is approximately equal to the sum of ε_{456} and ε_{546}. In contrast, 447 and 448 show an inverse isotope effect (positive values). Isotope ratios $^{17}O/^{16}O$ and $^{18}O/^{16}O$ follow mass-dependent fractionation as $\Delta^{17}O$ is close to 0‰; $\Delta^{17}O = (0.18 \pm 0.27)$‰. For the species 548, $\varepsilon_{p/s}$ is close to 0‰, as there was no significant change in the δ^{548} values during the reaction; see Tables A.1 and A.2 for the individual incubations at 20 °C and 30 °C, respectively. At higher incubation temperatures, smaller values of $\varepsilon_{p/s}$ for 456, 546, and 556 were observed (Table 1), while $\varepsilon_{p/s}$ for 447, 448, and 458 increased (absolute values).

Table 1
Enrichment factors $\varepsilon_{p/s}$ and intercepts derived from the Rayleigh model for N_2O production by the denitrifier *P. aureofaciens* at 20 °C and 30 °C. The uncertainty is expressed as expanded standard uncertainty at the 95% confidence interval. All values are given in ‰.

	20 °C		**30 °C**	
	$\varepsilon_{p/s}$	**intercept**	$\varepsilon_{p/s}$	**intercept**
ε_{456}	−40.3 ± 2.6	−4.2 ± 1.3	−35.1 ± 0.7	−3.5 ± 0.6
ε_{546}	−38.1 ± 3.4	−0.8 ± 1.0	−31.2 ± 0.6	1.6 ± 0.6
ε_{15bulk}	−39.1 ± 2.3	−2.6 ± 0.9	−33.2 ± 0.6	−0.9 ± 0.6
ε_{447}	21.3 ± 1.2	3.6 ± 0.4	24.5 ± 0.5	3.9 ± 0.5
ε_{448}	38.8 ± 1.5	7.6 ± 0.7	46.4 ± 1.2	7.6 ± 1.0
ε_{458}	−8.9 ± 2.0	4.2 ± 1.1	−11.7 ± 0.6	9.7 ± 0.5
ε_{548}	−3.4 ± 1.1	2.2 ± 0.4	−1.8 ± 0.5	11.4 ± 0.2
ε_{556}	−85.9 ± 1.5	−1.5 ± 0.6	−63.9 ± 1.4	−1.4 ± 1.3

Fig. 2a shows that there is a small but consistent temporal trend in SP as the reaction progresses. We also observed a similar temporal trend in the clumped signatures SP^{18} and the average abundance of 458 and 548 represented by $\Delta_{avg}^{458+548}$ (Fig. 2b,c). The temporal trends and values for Δ^{458} and Δ^{548} were similar, and they were therefore combined into $\Delta_{avg}^{458+548}$ for interpretation. For all parameters, the reaction is clearly outside of equilibrium conditions (Wang et al., 2004; Cao and Liu, 2012), which is indicated for $\Delta_{avg}^{458+548}$ by the grey bar in Fig. 2c (theoretical equilibrium $\Delta_{avg}^{458+548}$ values). Temporal changes in N_2O isotopic composition were particularly pronounced for the sampling after 1-day incubations (Fig. 2a,b,c; the data close to $[x] = 1$). Regarding the effect of incubation temperature, we observed differences in SP and SP^{18} of around 2‰ (Fig. 2a,b and Table 2) for incubations at 20 °C and 30 °C. For $\Delta_{avg}^{458+548}$, there was no significant effect of incubation temperature on the isotopic values (Fig. 2c and Table 2).

Finally, Fig. 2d provides Δ^{556} values as a function of the reaction progress. Values are mostly positive, they do not show a clear trend with respect to incubation temperature or reaction time, and they indicate variations between the duplicate incubations. Due to the large scatter in the Δ^{556} data, no conclusion on reaction reversibility during the N–N bond formation can be drawn (indicated by the grey bar for the reaction under thermal equilibrium).

4. DISCUSSION

The negative enrichment factors $\varepsilon_{p/s}$ for isotopocules 456, 546, 458, and 556 (Table 1) show that the isotopically lighter reaction intermediates react faster than the heavier ones. On the contrary, $\varepsilon_{p/s}$ for 447 and 448 indicate an inverse isotope effect, which is in accordance with the literature (Toyoda et al., 2005). The observed inverse isotope effect corresponds to preferential cleavage of the ^{16}O isotope in the sequential NO_3^- and NO_2^- reduction to NO. The O–exchange between intermediates in the NO_3^- reduction and H_2O can also affect δ^{447} and δ^{448} values of the produced N_2O (Casciotti et al., 2002). Smaller values of $\varepsilon_{p/s}$ for species 456, 546 and 556 at higher incubation temperature (Table 1) agree with previous findings for 456 and 546; e.g. Mariotti et al. (1981) reported smaller $\varepsilon_{15Nbulk}$ values (an average for the isotopomers 456 and 546) for soil samples incubated at 30 °C compared to those at 20 °C. This effect can be explained by an increase in the NO_3^- reduction rate with incubation temperature. Consequently, substrate transport (e.g., diffusion) into the enzyme active centre becomes rate-limiting and, therefore, fractionation associated with NO_3^- reduction is more limited. The temperature optimum for growth of *P. aureofaciens* likely lies between 28 °C and 30 °C (Hayn et al., 1956). Therefore, for our experiments, the reaction rate of NO_3^- reduction can be expected to be higher at 30 °C. This is confirmed by a distinct difference in the observed N_2O yields at both temperatures after the same incubation time (e.g., Table 2 – 91.0% at 20 °C and 100% at 30 °C for 7-day incubations). However, the magnitude of the resulting isotope effects is a product of a complex interplay between reaction rates for different reduction steps, transport rates into and out of

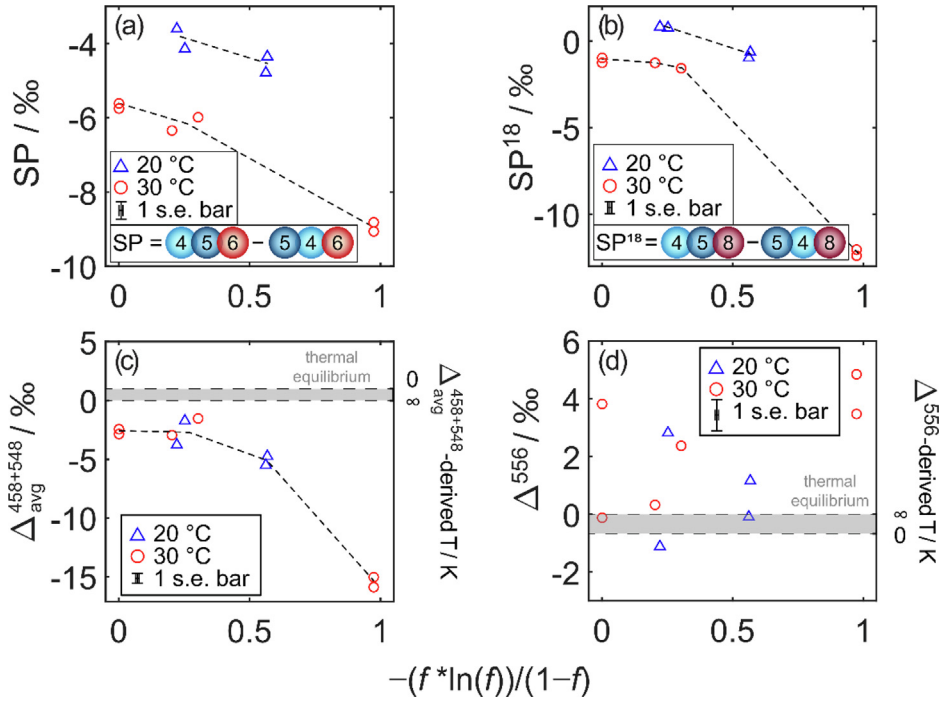

Fig. 2. Plots for **(a)** SP, **(b)** SP^{18}, **(c)** $\Delta^{458+548}_{avg}$, and **(d)** Δ^{556} of N_2O produced by *P. aureofaciens* as a function of the reaction progress expressed as $-(f\ln(f))/(1-f)$, where f is the fraction of remaining substrate. The reaction progress is from right to left. Dashed lines follow trends that are discussed in the main body of the text. Grey bars in plots (c) and (d) depict a narrow area of possible isotopic composition for N_2O that is formed under thermal equilibrium (based on theoretical calculations by Wang et al., 2004; Cao and Liu, 2012).

Table 2
N_2O isotopic composition at maximum NO_3^- conversion by *P. aureofaciens* at 20 °C and 30 °C, and comparison with results for *P. aeruginosa* by Magyar et al. (2016) (at 37 °C; Magyar, 2017). The indicated uncertainties are expressed as the standard error of the mean for the duplicate incubations (this study) or for the samples from triplicate incubations (Magyar et al., 2016). All isotopic values are given in ‰.

Sample	yield/%	$\delta^{15}N^{bulk}$	δ^{447}	δ^{448}	SP	SP^{18}	$\Delta^{458+548}_{avg}$
20 °C	91.0 ± 0.9	−11.8 ± 0.1	8.3 ± 0.1	16.1 ± 0.2	−3.9 ± 0.3	0.8 ± 0.3	−2.7 ± 0.3
30 °C	100	−1.7 ± 0.1	7.7 ± 0.1	15.3 ± 0.2	−5.7 ± 0.2	−1.1 ± 0.3	−2.6 ± 0.2
Magyar et al., 2016	100	−5.4 ± 0.2	25.1 ± 0.1	47.9 ± 0.1	−3.7 ± 0.3	−0.5 ± 3.8	0.4 ± 0.4

the cell, and exchange between substrate pools, all of which depend fundamentally on the incubation temperature. A model describing relationships between incubation temperature and isotopic fractionation has been developed for sulphate reduction, but is not trivial (Canfield et al., 2006). To the best of our knowledge, such a model currently does not exist for NO_3^- reduction.

The temporal trend in SP (Fig. 2a) agrees with the subtle (statistically insignificant) trend observed by Sutka et al. (2006); however, Haslun et al. (2018) indicated rather constant SP during the reaction. As previously discussed, slightly negative SP values can result from differences in $^{15}N/^{14}N$ fractionation between the two Fe binding atoms or inverse isotopic fractionation (^{15}N atoms react faster than ^{14}N) during the N–O bond breaking. In turn, we can deduce that ^{15}N–^{16}O bond breakage in the ^{16}O–^{14}N–^{15}N–^{16}O intermediate species is kinetically preferred over that of ^{14}N–^{16}O bond cleavage, which results in negative SP values ranging from −6‰ to −4‰ (Fig. 2a and Table 2). Interestingly, for both incubation temperatures, SP^{18} values are much closer to 0‰ than the SP values (Fig. 2b and Table 2). Following the argumentation above, SP^{18} values close to zero translate into a similar rate of ^{15}N–^{16}O bond breakage in the ^{18}O–^{14}N–^{15}N–^{16}O intermediate and ^{14}N–^{16}O bond breakage in the ^{16}O–^{14}N–^{15}N–^{18}O intermediate. For a mechanistic understanding of this effect, the strengths of the N–O bonds in O–N–N–O intermediates should be investigated theoretically in a future study.

Comparing $\Delta^{458+548}_{avg}$ with SP and SP^{18} (Fig. 2a,b,c), we found an increasing preference for moieties ^{15}N–^{16}O and ^{15}N–^{18}O as the reaction progresses, probably due to stronger bonding than in moieties with ^{14}N. Temporal changes in N_2O isotopic composition (Fig. 2a,b,c) may be related to large kinetic fractionation effects and deviation from thermodynamic equilibrium at the beginning of the reaction. This was observed by Haslun et al. (2018), where $\varepsilon_{p/s}$ values varied over the course of the experiment. A gradual change in $\varepsilon_{p/s}$ can occur in such a multi-step process due to the co-occurrence of multiple enzymatic steps and limitation by

product and/or substrate diffusion (Sutka et al., 2008). The $\varepsilon_{p/s}$ values may also depend on the extent of reaction reversibility. Alternatively, dynamics in the isotope behaviour might be driven by changes in microbial biomass or enzyme concentration (Maggi and Riley, 2010).

As mentioned above, SP and SP^{18} generally depend on the kinetic fractionation involved in the binding of the two NO molecules before the N–N bond formation or fractionation during the subsequent N–O bond breaking. Yang et al. (2014) attributed an increase in SP to normal kinetic isotope fractionation for the central N position and inverse fractionation for the terminal N position. Based on statistical thermodynamics calculations (Wang et al., 2004; Cao and Liu, 2012), SP and SP^{18} values around 47‰ and 45‰ are expected at 20 °C and 30 °C, respectively, for a thermodynamically equilibrated system. We assume that SP and SP^{18} values lower than that mean that the reaction is less reversible. Differences in SP and SP^{18} of around 2‰ (Table 2), which were observed for the incubations at 20 °C and 30 °C in the present study, can thus be attributed to less reversible NO reduction (which is more governed by reaction kinetics) with increasing temperature.

Table 2 shows a comparison of our results with those of Magyar et al. (2016), where N_2O was produced by the denitrifying bacteria *P. aeruginosa* with the same cNOR enzyme. In that work, little was discussed with regard to isotopic fractionation over the course of the reaction, temperature-related information, or possible reaction mechanisms. Nevertheless, values of SP, SP^{18}, $\Delta_{avg}^{458+548}$, and $\delta^{15}N^{bulk}$ in our study show good agreement with those by Magyar et al. (2016), while δ^{447} and δ^{448} differ, by approx. 17‰ and 33‰, respectively. This disagreement might be due to different reaction conditions or factors, including O isotopic composition of reaction substrates, equilibration of reaction substrates and intermediates with H_2O, O-branching effects, or incubation temperature (*P. aeruginosa*, as used by Magyar et al. (2016), was incubated at 37 °C; Magyar, 2017).

The observed fluctuations in Δ^{556} (Fig. 2d) might be partly caused by analytical uncertainties involved in repeated measurements by QCLAS, which has shown to be particularly challenging (Kantnerová et al., 2020b). However, uncertainties contributed by differences in individual incubations cannot be excluded. The value of Δ^{556} around 0‰ would indicate high reversibility during the N–N bond formation, as the two NO species ^{15}N–^{16}O and ^{15}N–O, which ultimately create the isotopocule 556 after cleavage of the O atom, are bound to the active site independently of each other. Theoretically, the resulting Δ^{556} is also expected to be close to the stochastic value of 0‰. For reactions in thermodynamic equilibrium, Wang et al. (2004) predicted Δ^{556} to be around zero (specifically −0.7‰ to 0.1‰). In addition, for denitrification-derived N_2O, Magyar (2017) predicted Δ^{556} of −0.01‰ using a simplified, statistical mechanical model of the cNOR active site, which was characterised by vibrational motions of NO bound to Fe in cNOR (based on the literature on spectroscopy of cNOR and similar proteins). The absence of negative values of Δ^{556} may confirm that no strong combinatorial effects are involved, as the ^{15}N site preference is close to zero (Yeung, 2016). Further interpretation of the Δ^{556} dataset presented here is beyond the scope of this study. The use of Δ^{556} values as indicators for specific reaction mechanisms requires further measurements under more controlled conditions.

5. CONCLUSION

This study reports on the three most abundant clumped isotope species of N_2O (458, 548, and 556) from the bacterial denitrification and discusses for the first time their temporal trends and enrichment factors. Measured isotope effects and temporal trends for the singly substituted isotopocules (456, 546, 447, and 448) show good agreement with previously published findings. Large kinetic isotope effects for the initial reaction period are observed in the temporal trends of the site preferences SP and SP^{18}. When the reaction is complete, SP^{18} is found to be close to 0‰, and the values of SP range between −6‰ and −4‰. Differences in SP and SP^{18} are interpreted in terms of the N–O bond breakage of the reaction intermediate O–N–N–O. The average abundance of the clumped isotopomers 458 and 548, $\Delta_{avg}^{458+548}$, follows a temporal trend similar to the trends of SP and SP^{18}. In addition, we studied the impact of incubation temperature on isotope fractionation and observed smaller isotope effects at higher incubation temperature (30 °C compared to 20 °C). Our dataset, in particular SP and SP^{18}, and the currently available hypotheses on the isotope signatures may support the *trans* reaction mechanism of the NO reduction to N_2O by the cNOR enzyme. However, further theoretical modelling and experimental data will be needed to conclude the ongoing dispute over the *cis* and *trans* reaction mechanisms.

Nevertheless, this work shows that clumped isotopes of N_2O provide new dimensions to the currently widely used isotope-mapping approaches, which might offer new insights into the sources and mechanisms of N_2O production that are not achievable using only singly substituted isotopocules. The clumped N_2O proxies SP^{18}, Δ^{556}, and Δ^{458} (or $\Delta_{avg}^{458+548}$) might also offer information about NO bonding to Fe atoms, the structures of transition states and reversibility of N–N binding reactions (SP^{18} and Δ^{556}) as well as the identification and extent of equilibration of reaction substrates (Δ^{458}). To apply these proxies for N_2O source partitioning in natural environments, further analyses of N_2O from other prominent source processes, e.g., nitrification, fungal denitrification, and abiotic NH_2-OH oxidation, under controlled reaction conditions (temperature, pH, etc.) are required. Key questions to solve in future research include constraining uncertainties in differences between SP and SP^{18} and obtaining additional information about ^{15}N–^{18}O abundance in nitrogen substrates using Δ^{458}. In parallel, a theoretical framework on the abiotic and enzymatic reaction mechanisms, including their clumped isotope signatures, must be developed to support the interpretation of experimental data.

Declaration of Competing Interest

The authors declare that they have no known competing financial interests or personal relationships that could have appeared to influence the work reported in this paper.

ACKNOWLEDGEMENTS

Funding: This work was supported by the Swiss National Science Foundation (grant number 200021_166255); the bilateral Japanese Swiss Science and Technology Program (JSPS International Fellowship for Research in Japan, grant number GR18108); and MEXT/JSPS KAKENHI (grant number JP17H06105).

The authors thank Nathaniel E. Ostrom, Laurence Yeung, an anonymous reviewer, and the Associate Editor Weifu Guo for constructive comments on the manuscript. We would like to thank Longfei Yu and Vít Svoboda for productive discussions and helpful contributions to the text.

APPENDIX A. SUPPLEMENTARY MATERIAL

Supplementary data to this article can be found online at https://doi.org/10.1016/j.gca.2022.05.006.

REFERENCES

Blomberg L. M., Blomberg M. R. A. and Siegbahn P. E. M. (2006) Reduction of nitric oxide in bacterial nitric oxide reductase—a theoretical model study. *Biochim. Biophys. Acta – Bioenerg.* **1757**, 240–252.

Blomberg M. R. A. (2017) Can reduction of NO to N_2O in cytochrome c dependent nitric oxide reductase proceed through a *trans*-mechanism? *Biochemistry* **56**, 120–131.

Butterbach-Bahl K., Baggs E. M., Dannenmann M., Kiese R. and Zechmeister-Boltenstern S. (2013) Nitrous oxide emissions from soils: how well do we understand the processes and their controls? *Philos Trans. R. Soc. B Biol. Sci.* **368**, 20130122–20130122.

Canfield D. E., Olesen C. A. and Cox R. P. (2006) Temperature and its control of isotope fractionation by a sulfate-reducing bacterium. *Geochim. Cosmochim. Acta* **70**, 548–561.

Cao X. and Liu Y. (2012) Theoretical estimation of the equilibrium distribution of clumped isotopes in nature. *Geochim. Cosmochim. Acta* **77**, 292–303.

Casciotti K. L., Böhlke J. K., McIlvin M. R., Mroczkowski S. J. and Hannon J. E. (2007) Oxygen isotopes in nitrite: analysis, calibration, and equilibration. *Anal. Chem.* **79**, 2427–2436.

Casciotti K. L., Sigman D. M., Hastings M. G., Böhlke J. K. and Hilkert A. (2002) Measurement of the oxygen isotopic composition of nitrate in seawater and freshwater using the denitrifier method. *Anal. Chem.* **74**, 4905–4912.

van Dijk J., Fernandez A., Bernasconi S. M., Caves Rugenstein J. K., Passey S. R. and White T. (2020) Spatial pattern of super-greenhouse warmth controlled by elevated specific humidity. *Nat. Geosci.* **13**, 739–744.

Eiler J. M. (2007) "Clumped-isotope" geochemistry – The study of naturally-occurring, multiply-substituted isotopologues. *Earth Planet. Sci. Lett.* **262**, 309–327.

Eiler J. M. (2013) The Isotopic Anatomies of Molecules and Minerals. *Annu. Rev. Earth Planet. Sci.* **41**, 411–441.

Fehling C. (2012) *Mechanistic insights from the ^{15}N-site preference of nitrous oxide utilizing high resolution near-infrared cw cavity ringdown spectroscopy and Density Functional Theory calculations*. Kiel University, PhD thesis.

Frame C. and Casciotti K. (2010) Biogeochemical controls and isotopic signatures of nitrous oxide production by a marine ammonia-oxidizing bacterium. *Biogeosciences* **7**, 2695–2709.

Haslun J. A., Ostrom N. E., Hegg E. L. and Ostrom P. H. (2018) Estimation of isotope variation of N_2O during denitrification by *Pseudomonas aureofaciens* and *Pseudomonas chlororaphis*: implications for N_2O source apportionment. *Biogeosciences* **15**, 3873–3882.

Hattori S., Savarino J., Kamezaki K., Ishino S., Dyckmans J., Fujinawa T., Caillon N., Barbero A., Mukotaka A., Toyoda S., Well R. and Yoshida N. (2016) Automated system measuring triple oxygen and nitrogen isotope ratios in nitrate using the bacterial method and N_2O decomposition by microwave discharge. *Rapid Commun. Mass Spectrom.* **30**, 2635–2644.

Hayn W. C., Stodola F. H., Locke J. M., Pridham T. G., Conway H. F., Sohns V. E. and Richard Jackson An W. (1956) *Pseudomonas aureofaciens* Kluyver and phenazine α-carboxylic acid, its characteristic pigment. *J. Bacteriol.* **72**, 412–417.

He Y., Cao X. and Bao H. (2020) Ideas and perspectives: The same carbon behaves like different elements-an insight into position-specific isotope distributions. *Biogeosciences* **17**, 4785–4795.

Hino T., Matsumoto Y., Nagano S., Sugimoto H., Fukumori Y., Murata T., Iwata S. and Shiro Y. (2010) Structural basis of biological N_2O generation by bacterial nitric oxide reductase. *Science* **330**, 1666–1670.

Kaiser J., Röckmann T. and Brenninkmeijer C. A. M. (2003) Assessment of $^{15}N^{15}N^{16}O$ as a tracer of stratospheric processes. *Geophys. Res. Lett.* **30**, 16–19.

Kantnerová K. (2020) *Analysis of clumped isotopes in nitrous oxide: method development and first applications*. ETH Zurich, PhD thesis.

Kantnerová K., Jespersen M. F., Bernasconi S. M., Emmenegger L., Johnson M. S. and Mohn J. (2020a) Photolytic fractionation of seven singly and doubly substituted nitrous oxide isotopocules measured by quantum cascade laser absorption spectroscopy. *Atmos. Environ. X* **8**, 100094.

Kantnerová K., Yu L., Zindel D., Zahniser M. S., Nelson D. D., Tuzson B., Nakagawa M., Toyoda S., Yoshida N., Emmenegger L., Bernasconi S. M. and Mohn J. (2020b) First investigation and absolute calibration of clumped isotopes in N_2O by mid-infrared laser spectroscopy. *Rapid Commun. Mass Spectrom.* **34**, e8836.

Labidi J., Barry P. H., Bekaert D. V., Broadley M. W., Marty B., Giunta T., Warr O., Sherwood L. B., Fischer T. P., Avice G., Caracausi A., Ballentine C. J., Halldórsson S. A., Stefánsson A., Kurz M. D., Kohl I. E. and Young E. D. (2020) Hydrothermal $^{15}N^{15}N$ abundances constrain the origins of mantle nitrogen. *Nature* **580**, 367–371.

Maggi F. and Riley W. J. (2010) Mathematical treatment of isotopologue and isotopomer speciation and fractionation in biochemical kinetics. *Geochim. Cosmochim. Acta* **74**, 1823–1835.

Magyar P. M. (2017) *Insights into pathways of nitrous oxide generation from novel isotopologue measurements*. California Institute of Technology, PhD thesis.

Magyar P. M., Orphan V. J. and Eiler J. M. (2016) Measurement of rare isotopologues of nitrous oxide by high-resolution multi-collector mass spectrometry. *Rapid Commun. Mass Spectrom.* **30**, 1923–1940.

Mariotti A., Germon J. C., Hubert P., Kaiser P., Letolle R., Tardieux A. and Tardieux P. (1981) Experimental determination of nitrogen kinetic isotope fractionation: Some principles;

illustration for the denitrification and nitrification processes. *Plant Soil* **62**, 413–430.

Ono S., Wang D. T., Gruen D. S., Lollar B. S., Zahniser M. S., McManus B. J. and Nelson D. D. (2014) Measurement of a doubly substituted methane isotopologue, $^{13}CH_3D$, by tunable infrared laser direct absorption spectroscopy. *Anal. Chem* **86**, 6487–6494.

Prokhorov I., Kluge T. and Janssen C. (2019) Optical clumped isotope thermometry of carbon dioxide. *Sci. Rep.* **9**, 1–11.

Raman S., Ashcraft R. W., Vial M. and Klasky M. L. (2005) Oxidation of hydroxylamine by nitrous and nitric acids. Model development from first principle SCRF calculations. *J. Phys. Chem. A* **109**, 8526–8536.

Sigman D. M., Casciotti K. L., Andreani M., Barford C., Galanter M. and Böhlke J. K. (2001) A bacterial method for the nitrogen isotopic analysis of nitrate in seawater and freshwater. *Anal. Chem.* **73**, 4145–4153.

Stolper D. A., Martini A. M., Clog M., Douglas P. M., Shusta S. S., Valentine D. L., Sessions A. L. and Eiler J. M. (2015) Distinguishing and understanding thermogenic and biogenic sources of methane using multiply substituted isotopologues. *Geochim. Cosmochim. Acta* **161**, 219–247.

Sutka R. L., Adams G. C., Ostrom N. E. and Ostrom P. H. (2008) Isotopologue fractionation during N_2O production by fungal denitrification. *Rapid Commun. Mass Spectrom.* **22**, 3989–3996.

Sutka R. L., Ostrom N. E., Ostrom P. H., Breznak J. A., Gandhi H., Pitt A. J. and Li F. (2006) Distinguishing nitrous oxide production from nitrification and denitrification on the basis of isotopomer abundances. *Appl. Environ. Microbiol.* **72**, 638–644.

Sutka R. L., Ostrom N. E., Ostrom P. H., Gandhi H. and Breznak J. A. (2003) Nitrogen isotopomer site preference of N_2O produced by *Nitrosomonas europaea* and *Methylococcus capsulatus*. *Bath. Rapid Commun. Mass Spectrom.* **17**, 738–745.

Timóteo C. G., Pereira A. S., Martins C. E., Naik S. G., Duarte A. G., Moura J. J. G., Tavares P., Huynh B. H. and Moura I. (2011) Low-spin heme b_3 in the catalytic center of nitric oxide reductase from *Pseudomonas nautica*. *Biochemistry* **50**, 4251–4262.

Toyoda S., Mutobe H., Yamagishi H., Yoshida N. and Tanji Y. (2005) Fractionation of N_2O isotopomers during production by denitrifier. *Soil Biol. Biochem.* **37**, 1535–1545.

Toyoda S., Yoshida N. and Koba K. (2017) Isotopocule analysis of biologically produced nitrous oxide in various environments. *Mass Spectrom. Rev.* **36**, 135–160.

Wang D. T., Gruen D. S., Lollar B. S., Hinrichs K., Stewart L. C., Holden J. F., Hristov A. N., Pohlman J. W., Morrill P. L., Könneke M., Delwiche B., Reeves E. P., Sutcliffe C. N., Ritter D. J., Seewald J. S., Delwiche K. B., Reeves E. P., Sutcliffe C. N., Ritter D. J., Seewald J. S., McIntosh J. C., Hemond H. F., Kubo M. D., Cardace D., Hoehler T. M. and Ono S. (2015) Nonequilibrium clumped isotope signals in microbial methane. *Science* **348**, 428–431.

Wang Z., Schauble E. A. and Eiler J. M. (2004) Equilibrium thermodynamics of multiply substituted isotopologues of molecular gases. *Geochim. Cosmochim. Acta* **68**, 4779–4797.

Watmough N. J., Field S. J., Hughes R. J. L. and Richardson D. J. (2009) The bacterial respiratory nitric oxide reductase. *Biochem. Soc. Trans.* **37**, 392–399.

Werner R. A. and Brand W. A. (2001) Referencing strategies and techniques in stable isotope ratio analysis. *Rapid Commun. Mass Spectrom.* **15**, 501–519.

Yang H., Gandhi H., Ostrom N. E. and Hegg E. L. (2014) Isotopic fractionation by a fungal P450 nitric oxide reductase during the production of N_2O. *Environ. Sci. Technol.* **48**, 10707–10715.

Yeung L. Y. (2016) Combinatorial effects on clumped isotopes and their significance in biogeochemistry. *Geochim. Cosmochim. Acta* **172**, 22–38.

Yeung L. Y., Ash J. L. and Young E. D. (2015) Biological signatures in clumped isotopes of O_2. *Science* **348**, 431–434.

Yeung L. Y., Haslun J. A., Ostrom N. E., Sun T., Young E. D., Van Kessel M. A. H. J., Lücker S. and Jetten M. S. M. (2019a) In situ quantification of biological N_2 production using naturally occurring $^{15}N^{15}N$. *Environ. Sci. Technol.* **53**, 5168–5175.

Yeung L. Y., Li S., Kohl I. E., Haslun J. A., Ostrom N. E., Hu H., Fischer T. P., Schauble E. A. and Young E. D. (2017) Extreme enrichment in atmospheric $^{15}N^{15}N$. *Sci. Adv.* **3**, eaao6741.

Yeung L. Y., Murray L. T., Martinerie P., Witrant E., Hu H., Banerjee A., Orsi A. and Chappellaz J. (2019b) Isotopic constraint on the twentieth-century increase in tropospheric ozone. *Nature* **570**, 224–227.

York D. (1969) Least squares fitting of a straight line with correlated errors. *Earth Planet. Sci. Lett.* **5**, 320–324.

Zumft W. G. (1997) Cell biology and molecular basis of denitrification. *Microbiol. Mol. Biol. Rev.* **61**, 533–616.

Associate editor: Weifu Guo